

# Accretion Signatures from Massive Young Stellar Objects<sup>1</sup>

R. D. Blum

*Cerro Tololo Interamerican Observatory, Casilla 603, La Serena, Chile*  
*rblum@ctio.noao.edu*

C. L. Barbosa & A. Daminieli

*Instituto de Astronomia, Geofísica e Ciências Atmosféricas - USP, Rua do Matão, 1226*  
*Cid. Universitária São Paulo-SP CEP 05508-900, São Paulo, Brasil*  
*cassio@astro.iag.usp.br, daminieli@astro.iag.usp.br*

P. S. Conti

*JILA, University of Colorado*  
*Campus Box 440, Boulder, CO, 80309*  
*pconti@jila.colorado.edu*

S. Ridgway

*National Optical Astronomy Observatory, 950 N. Cherry Street, Tucson, AZ, 85719*  
*sridgway@noao.edu*

## ABSTRACT

High resolution ( $\lambda/\Delta\lambda = 50,000$ )  $K$ -band spectra of massive, embedded, young stellar objects are presented. The present sample consists of four massive young stars located in nascent clusters powering Galactic giant H II regions. Emission in the  $2.3\ \mu\text{m}$  2–0 vibrational–rotational bandhead of CO is observed. A range of velocity broadened profiles seen in three of the objects is consistent with the emission arising from a circumstellar disk seen at various inclination angles.  $\text{Br}\gamma$  spectra of the same spectral and spatial resolution are also presented which support an accretion disk or torus model for massive stars. In the fourth object, Br emission suggesting a rotating torus is observed, but the CO profile is narrow, indicating that there may be different CO emission mechanisms in massive stars and this is consistent with earlier observations of the BN object and MWC 349. To–date, only young massive stars of late O or early B types have been identified with clear accretion disk signatures in such embedded clusters. Often such stars are found in the presence of other more massive stars which are revealed by their photospheric spectra but which exhibit no disk signatures.

This suggests the timescale for dissipating their disks is much faster than the less massive OB stars or that the most massive stars do not form with accretion disks.

*Subject headings:* H II regions — infrared: stars — stars: early-type — stars: fundamental parameters — stars: formation

## 1. INTRODUCTION

How do massive stars form? Simple expectations based on the observed masses and life times of massive stars dictate that the timescale for formation must be much shorter than for low mass stars and that the average mass accretion rates must be high ( $\sim 10^{-4} M_{\odot} \text{ yr}^{-1}$ ). Detailed calculations suggest the formation timescale is approximately  $10^5 \text{ yr}$  (McKee & Tan 2003). In contrast to low mass stars which are more numerous and whose formation proceeds by distinct and identifiable phases of longer timescales, high mass stars are rare, their formation rapid and obscured by an overlying envelope. It is also unavoidable that a massive core will form and begin evolving (converting H to He) while the larger protostar is still accreting material. This makes for theoretical complexity as well as observational difficulty.

Despite these difficulties, progress is being made on both theoretical and observational fronts; see the recent reviews by Garay & Lizano (1999), Kurtz et al. (2000), and Churchwell (2002). A number of groups have developed accretion models for massive stars: Behrend & Maeder (2001), Yorke & Sonnhalter (2002), and McKee & Tan (2003). Observational evidence for accretion disks has been accumulating through mm and molecular line measurements for a few highly embedded objects (Garay & Lizano 1999; Shepherd & Kurtz 1999). While massive protostars, these objects are not of the most massive type but tend to be mid to early B stars. Methanol masers have been used to trace sites of massive star formation, and have been proposed to trace circumstellar accretion disks (Norris et al. 1998; Phillips et al. 1998) though there are alternate explanations (Walsh et al. 1998). A recent

---

<sup>1</sup>Based on observations obtained at the Gemini Observatory, which is operated by the Association of Universities for Research in Astronomy, Inc., under a cooperative agreement with the NSF on behalf of the Gemini partnership: the National Science Foundation (United States), the Particle Physics and Astronomy Research Council (United Kingdom), the National Research Council (Canada), CONICYT (Chile), the Australian Research Council (Australia), CNPq (Brazil) and CONICET (Argentina)

survey of these objects for molecular outflows ( $\text{H}_2$  emission), which are expected to be associated with the putative disks, also argues against the disk origin for methanol emission (De Buizer 2003).

Another possible formation mechanism for massive stars is through mergers of lower mass protostars in a dense cluster environment. Recent simulations have been successful in producing massive stars through this mechanism (Bonnell et al. 1998; Stahler et al. 2000; Bonnell & Bate 2002). The details of the Bonnell & Bate (2002) simulation show that the stellar cluster density evolves rapidly at the end of the formation process reaching densities suitable for mergers. This suggests it will be difficult to catch a massive star “in the act” and so direct observational confirmation of merger formation of the most massive stars may be very difficult. On the other hand, lack of detection of accretion signatures for the most massive stars can be used to infer the mass at which mergers would become the dominant channel of formation. This would also require substantial observational effort.

Obviously, investigations of the earliest phases of massive star formation have centered around longer wavelengths which penetrate the large column depth of material surrounding massive protostars. But current angular resolutions and sensitivities achievable restrict study to the relatively few nearby sources (the ALMA telescope will help to rectify this situation!). In the present work we take advantage of the fact that newly formed massive stars, or massive young stellar objects (MYSOs), while at the tail end of the star birth process, can be used to search for evidence of remnant accretion disks. Our ongoing survey of Galactic giant H II (GHII) regions in the near infrared (Blum et al. 1999, 2000, 2001; Conti & Blum 2002; Figuerêdo et al. 2002, 2004) combined with the work of Hanson et al. (1997) has led to the discovery of a sample of MYSOs with potential disk signatures which we describe below. These candidates have been observed at high angular and spectral resolution in a variety of  $K$ – band emission lines. In this paper, we discuss the observations of  $\text{Br}\gamma$  and (in more detail)  $\text{CO } 2.3 \mu\text{m}$  emission. The latter can be particularly useful in studying the circumstellar geometry of MYSOs as has been shown to be the case for low mass YSOs (Carr 1989; Carr et al. 1993; Chandler et al. 1993, 1995; Najita et al. 1996).

## 2. OBSERVATIONS AND DATA REDUCTION

### 2.1. Sample Selection

Our sample of stars consists of  $K$ –band bright and  $H - K$  red objects found in our imaging survey of GHII regions (Table 1) and the study of M17 by Hanson et al. (1997). These objects are often the brightest near infrared sources in the associated clusters and have

colors which indicate strong excess emission. None of these stars have  $K$ -band photospheric features present in low resolution spectra, but all are probably late O or early B type stars based on other (primarily luminosity) arguments; see the references listed in Table 1. The complete sample of such massive stars still enshrouded by their birth material and for which at least low resolution spectra are available is currently about 10 (our survey is still on-going). In this paper, we present high spectroscopic resolution data for four of the stars which show CO 2.3  $\mu\text{m}$  2–0 vibrational rotational bandhead emission in their low resolution spectra.

## 2.2. Gemini/Phoenix Observations

The target spectra were obtained with the NOAO Phoenix spectrometer on the Gemini South 8m telescope in 2002 and 2003 (see Table 1). Phoenix is described in detail by Hinkle et al. (2003). In all cases the data were obtained with the four pixel (0.32") wide slit giving a resolution of  $\lambda/\Delta\lambda \approx 50,000$ . The resolution element is over-sampled in this mode giving approximately five pixels per element. The Phoenix pixel scale on Gemini South is approximately 0.09"  $\text{pix}^{-1}$  resulting in a slit length of about 15".

Spectra were obtained in both photometric and non-photometric conditions and for both Br $\gamma$  (2.1661  $\mu\text{m}$ , all wavelengths in this paper are quoted in vacuum) and the first overtone CO 2–0 bandhead (2.2935  $\mu\text{m}$ ). For one star, NGC3576 #48, two grating settings near the CO line were obtained. All other stars have data for one grating setting only. The seeing (at  $K$ ) ranged from approximately 0.4" to 1.3". Typically it was close to 0.5", with the exception of the Br $\gamma$  observations for NGC3576 #48 (1" – 1.3"). A similar spectrum of NGC3576 #48 at the position of Br $\alpha$  was also obtained on the same night.

The two-dimensional long slit images were reduced with the IRAF<sup>2</sup> data reduction package. Each image was divided by a flat field image obtained with the Gemini GCAL unit and then subtracted by a sky image. The Br data had independent sky frames observed off the targets since the emission often filled the entire slit. The CO sky frames were obtained by nodding the target along the slit by about half a slit length (i.e. the target was always on the slit) since the CO emission was spatially unresolved and centered on the point source. The Br images were obtained with N–S and/or E–W slit orientation on the sky, while the CO data always had a E–W orientation.

---

<sup>2</sup>IRAF is distributed by the National Optical Astronomy Observatories, which are operated by the Association of Universities for Research in Astronomy, Inc., under cooperative agreement with the National Science Foundation.

After extracting one-dimensional spectra (with  $\pm 2$  to 5 pixels along the slit  $\sim 0.2''$  to  $0.5''$ ), the spectra were divided by similar spectra obtained on atmospheric standard stars. For the Br spectra, intrinsic absorption in the standards was removed by fitting the absorption features dividing the fit into the original spectra. The final ratioed spectra were wavelength calibrated using telluric absorption lines measured off the electronic version of the NOAO Arcturus atlas (Hinkle, Wallace, & Livingston 1995). A linear fit to the telluric line positions gives a typical uncertainty of about  $\pm 0.5$  to 1.0 pixel (i.e. 1/10th to 1/5th of a resolution element), or  $\pm 0.7$  to 1.3 km s<sup>-1</sup>.

### 3. RESULTS

#### 3.1. CO Emission

The individual spectra are shown in Figures 1, 2, 3, and 4. The spectra have been binned by a factor of three to improve the signal to noise and the continuum has been subtracted. These spectra show a range of profiles from narrow emission (NGC3576 #48, Figure 1) to very broad emission (M17–268, Figure 2).

The shape of the CO emission profile in these spectra is the same as that expected for a rotating Keplerian disk. In particular, Figure 2 shows a profile for M17–268 which is a good match to the profile for the lower mass stars analyzed by Carr et al. (1993), Chandler et al. (1995), and Najita et al. (1996). As discussed by Carr et al. (1993), the pronounced blue-shifted shoulder and redshifted emission peak are well fit by a rotating disk.

Following the procedure outlined by Kraus et al. (2000), we fit the emission profiles of each of the four massive stars in our sample. These models use power-laws in the disk temperature and surface density distributions with optical depth and flux in the CO transitions calculated in each cell of a radial plus azimuthal coordinate grid. The emission from each cell is added to the final spectrum according to its rotational velocity and inclination. Within each cell, an intrinsic line profile is assumed. Following Najita et al. (1996), we have adopted a Lorentzian profile (which allows for lower column densities; see Najita et al. 1996), though Gaussian profiles of larger width can also fit the data. In the range of wavelengths covered by the present Phoenix spectra, the Hydrogen Pfund lines are expected to be weak (see Kraus et al. 2000).

We adopt a temperature of 5000 K (above which CO should be dissociated) at the inner radius of the CO emission zone. The column of material emitting is assumed to be geometrically thin with uniform temperature and density in the direction normal to the disk so that the optical depth through any cell in the disk is just the absorption coefficient for a

single CO molecule times the total surface density ( $\text{cm}^{-2}$ ). We do not fit the continuum, only the line emission. Similar models which consider a two temperature disk (i.e. the structure normal to the disk plane has two components) with an emission component overlying a continuum component have been constructed by Najita et al. (1996). For the purpose of the exploring the kinematic signatures of the disks, a single emission component is sufficient.

The observed profiles were fit by systematically varying the free parameters. To obtain a rough fit, the parameters were varied and the results compared by eye to the observed spectra. The free parameters are the temperature distribution exponent,  $p$ , the density distribution exponent,  $q$ , the total column density at the inner radius for emission,  $N_{\text{CO}}$ ,  $v_{\text{ini}}$  at the inner radius, the systemic velocity of the system, the width of the intrinsic line profile, and the ratio of outer to inner radius,  $\beta$ . In practice, the fits are not very sensitive to the value of  $p$  and it was fixed for all models to 0.5. Good fits were obtained in all cases with the adopted profile width of  $1 \text{ km s}^{-1}$  (see above). Once the initial parameters were obtained by eye, we improved the fits using a simple grid search method, minimizing Chi square as described in Bevington & Robinson (1992). For the Chi square minimization, the values of  $q$ ,  $\beta$ ,  $v_{\text{ini}}$ , and  $N_{\text{CO}}$  were varied in turn and the minimum Chi square found for each independently. The procedure was iterated one time with the reduced Chi square changing by less than 1% in all cases. The reduced Chi square values ranged from 0.75 to 1.4. The parameters are summarized in Table 2, and the best fits obtained by a systematic variation of the free parameters are shown as the smooth black lines in each of Figures 1, 2, 3, and 4. The formal one sigma errors on the fitted parameters are quite small, and the models clearly fit the data well as seen in Figures 1, 2, 3, and 4. However, a more detailed treatment including more CO transitions would be required to definitively explore the physical state of these disks. The goal of the present simplified treatment is to show that plausible kinematic models of rotating disks fit the CO profiles well.

The systemic velocity was determined by cross-correlation of the model and observed profiles using the IRAF "rv" package. The cross-correlation peak center region was fit in each case with a Gaussian, and the formal error in its center is less than one pixel in all cases. We have added to this uncertainty (in quadrature) the typical uncertainty cited above (§2) from the wavelength solution.

For NGC3576 #48, there is essentially an additional parameter which is the relative flux level between the two grating positions. The region where the two pieces are spliced together is also unreliable due to bad pixel rows at the end of the detector. There appears to be a slight over-subtraction of the continuum at the red end.

### 3.2. Br $\gamma$ Emission

Unlike CO emission which is spatially unresolved, the Br $\gamma$  emission is typically extended along the slit in our 2–D images. The ionization can be due to the central source and/or other sources. In Figure 5, we display the long slit images for NGC3576 #48, M17–268, and M17–275. The spatial dimension runs along the horizontal axis, and the spectral or dispersion dimension runs along the vertical axis. These images are rectified (shifted so the spectrum runs vertically in the image), spatially shifted, and combined images which cover up to 24" along the slit (a single exposure corresponds to a 15" slit). Contours derived from the same images are overlaid on the gray scale to indicate the relative strength of emission along the slit and compared to the continuum source. The gray scale itself has been stretched to show faint detail in the emission morphology.

The emission away from the central source of NGC3576 #48 is intense, peaking  $\sim 4''$  (0.05 pc, for  $d = 2800$  pc, de Pree, Nysewander, & Goss 1999) south of the continuum source in the N–S image (see Figure 5). There is a somewhat lower “plateau” of emission out to 6.5" (0.09 pc) south which then decreases sharply to a relatively low value at 9.4" (0.13 pc) south. Beyond this point, the emission may increase again. To the north, the emission is much less intense, only a maximum of 6% of the peak; again, a clear cutoff is apparent at about 8" (0.11 pc) north. An E–W slit spectrum was also taken. In the E–W case, the emission is much stronger on the west side of the continuum source, peaking at 9" (0.12 pc) west (see Figure 5). The emission centered on the source in both slit orientations shows a double peak and is also strong, about 34% and 43% of the peak in the E–W and N–S orientations, respectively. The two velocity extremes have a peak–to–peak difference of about  $85 \text{ km s}^{-1} \pm 1.5 \text{ km s}^{-1}$  in each case, and the mean velocity of this compact or “torus” component appears blue–shifted from the bright off source emission to the south and west. The compact emission is interpreted as a rotating torus below.

Br $\gamma$  spectra for NGC3576 #48, M17–268, and M17–275 are shown in Figures 6, 8, and 9, respectively (we were unable to obtain a spectrum of G333.1–0.4 #4). These spectra were extracted from the original individual frames, not the 2–D images shown in Figure 5. Each spectrum is an extraction over the central  $\sim 0.3$  to 1" by 0.32" slit width. The emission in the NGC3576 #48 slits is highly variable, and this precluded using background apertures to isolate the emission close to the stellar source. However, the emission is strong at the position of the source and should therefore be representative of the circumstellar component. This is supported by the similarity of the spectrum extracted from the N–S and E–W slits. Because the emission in the M17 sources is more uniform across the sources, background apertures could be used. Figure 8 and 9 show the total emission seen through the Phoenix slit and the spatially compact component obtained by subtracting the uniform component

using  $0.9''$  wide apertures parallel to the continuum source and located at  $\pm 1.3''$  away. In each case, a relatively strong but narrow emission component is removed leaving a much broader component which arises from a region close to the central star.

Table 3 summarizes the  $\text{Br}\gamma$  velocities for the central compact emission component(s). For each source, there is a mean  $\text{Br}\gamma$  velocity, fullwidth, and peak-to-peak velocity difference (M17-268 and NGC3576 #48). These parameters were determined by least squares fitting to Lorentzian or Gaussian profiles. The formal uncertainties are less than 1 pixel. In practice, the setting of the continuum dominates the uncertainty in the fit. For a range of continuum choices, the fits suggest centroids which vary by approximately  $\pm$  two pixels. The typical residual in the position of lines used in the wavelength solution (one pixel) is added in quadrature to this value. The FWHM are similarly affected by the continuum choice. The peak-to-peak separations for NGC3576#48 and M17-268 were determined by calculating the centroids of the individual peaks. The formal uncertainty is taken conservatively as the typical residual in the wavelength solution (one pixel).

He I 7-4 emission is present in each case to the blue of  $\text{Br}\gamma$  (about 1/4 of the way from the top of each image). The rest wavelength of the emission is  $2.1647 \mu\text{m}$  (Figer et al. 1997) and its presence clearly establishes the “hot” nature of the central sources. The He I peak-to-peak velocity is  $93 \pm 1.5 \text{ km s}^{-1}$  compared to  $85 \pm 1.5 \text{ km s}^{-1}$  for  $\text{Br}\gamma$  in NGC3576 #48 (the mean velocities are equal within the one sigma uncertainties) which suggests the He I emission arises from a region slightly closer to the central source in models where the emission arises due to rotation (see below).

## 4. DISCUSSION

### 4.1. The Origin of the CO Emission in MYSOs

Scoville et al. (1983) presented high resolution spectra of the Becklin-Neugebauer (BN) object which show many similarities to the spectra presented here. In particular, BN exhibits strong Brackett series emission and CO  $2.3 \mu\text{m}$  emission. BN is also thought to be a heavily shrouded early B-type star. In their analysis of BN, Scoville et al. (1983) preferred an interpretation for the observed narrow CO emission which was not produced in a rotating circumstellar disk. Except for the case where BN was viewed nearly face on, the small required area, and hence radius, of the bandhead emission region requires a high rotational velocity which is not observed. Scoville et al. (1983) proposed a shock model for the origin of the CO emission instead, placing this physically narrow region much farther from the star.

Carr et al. (1993) and Chandler et al. (1995) modeled the CO emission from other



young stars, including several with masses up to  $\sim 25 M_{\odot}$ , and found excellent fits for a disk origin. Chandler et al. (1995) also compared their data to wind models, but found that the disk models generally fit better. The CO profiles in our spectra of M17–268, M17–275, and G333.1–0.4 #4 are very well fit by emission arising in a Keplerian rotating disk with  $v_{\text{ini}}$  between about  $100 \text{ km s}^{-1}$  and  $260 \text{ km s}^{-1}$ . For the estimated masses given in Table 2, this requires the CO emission to arise at radii less than 1 AU from the central star in all cases. Each has a profile which exhibits the characteristic shape of CO emission produced by a Keplerian disk (Carr et al. 1993; Chandler et al. 1995), including most notably, the blue shoulder and redshifted emission peak. The case for massive star formation of late O and early B stars by accretion seems quite solid. NGC3576#48, on the other hand, shows a very narrow profile which could be consistent with either a disk seen nearly face-on or with some other geometry such as a wind or inflow/outflow.

Is BN a special case? Besides our spectrum of NGC3576 #48, a similar spectrum of the  $2.3 \mu\text{m}$  first overtone emission is presented by Kraus et al. (2000) for the MYSO MWC 349. The narrow emission is difficult to fit with a disk model or a combination disk plus wind. This is because Kraus et al. (2000) fix the inclination of the disk to be nearly edge on, based on independent measurements of ionized hydrogen lines and radio continuum (Rodríguez & Bastian 1994). For such a geometry, the narrow CO emission profile results in an emission region which is far from the central source where the temperature and surface density are expected to be much lower based on observations of the associated dust disk.

The observations presented here for NGC3576 #48 also show narrow CO emission (Figure 1). In this case, the observed profile could be due to inclination effects. However, the  $\text{Br}\gamma$  emission depicted in Figures 5 and 6 shows a double peaked profile with a velocity separation between peaks of  $85 \text{ km s}^{-1}$ . This profile could arise from an expanding shell or rotating torus. Similar profiles occur in MWC 349 (Hamann & Simon 1986) for a variety of lines including  $\text{Br}\gamma$ . The  $\text{Br}\gamma$  emission in MWC 349 has a peak-to-peak velocity difference of about  $50 \text{ km s}^{-1}$ . In the case of MWC 349, Hamann & Simon (1986) interpret the emission as arising from the ionized face of a circumstellar disk. Barbosa et al. (2003) developed a flared torus model for NGC3576 #48 in order to explain the differences in the observed spectral energy distributions of NGC3576 #48 and several other sources in the same cluster.

In both NGC3576 #48 and MWC 349, a natural expectation is that the CO emission would be produced in the inner warm, neutral component of such a disk or torus. Kraus et al. (2000) have suggested a model which qualitatively reconciles this expectation for MWC 349 with the observed narrow CO profile. In their model, the large scale circumstellar geometry is taken as a bulging disk. The bulged disk shadows much of the CO emitting region in the inner part of the disk (for inclinations nearly edge-on) allowing only a view toward a small

sector which limits the range of observed velocities (see Figure 17 of Kraus et al. 2000). Material from the ionized portion of the disk, which is ablated off of it, fills the region above the disk and is thus visible (consistent with the photo-ablation models of Hollenbach et al. 1994). This material carries the kinematic signature of the rotating disk it arises from (Hamann & Simon 1986).

While the model of Kraus et al. (2000) limits the range of velocities seen in the CO bandhead emission, the mean velocity should be unaffected. In the case of NGC3576 #48, the mean CO velocity is better matched to the bulk of the redshifted Br $\gamma$  emission, and not that of the compact, double-peaked Br $\gamma$  emission presumably arising in the torus (Table 2). The mean velocity of the CO and bulk Br $\gamma$  emission are also in agreement with the radio recombination line peak emission velocity for NGC3576 as given by de Pree et al. (1999).

With reference to the near infrared images of NGC3576 #48 presented by Figuerêdo et al. (2002), the following picture emerges. The source is clearly breaking out of its birth material. The images indicate that a “cap” of material running along the north side of the object provides a column of obscuration in that direction along the line of sight. The bulk of the cloud is to the south, but the immediate vicinity of NGC3576 #48 is cleared away in this direction providing a view inside the cavity and beyond #48; the cavity itself appears to be expanding and breaking up due to the action of #48 and other sources in the cluster. Barbosa et al. (2003) suggest the main part of the cluster is located to the SW of #48 and obscured from our line of sight at these wavelengths. This geometry is consistent with the velocities and spatial distribution of the Br $\gamma$  emission seen in Figure 5. The emission to the south (*farleft* panel) in Figure 5 is much stronger than to the north. The “cap” mentioned above shields the back side of the cavity which is evidently being pushed away along our line of sight. The emission is not uniform in the E–W direction, but much more emission is seen on both east and west sides than in the north–south case. The blue shifted emission to the north must originate on the inner wall of the “cap.” This part of the cavity wall is being pushed toward us along the line of sight. Further support for this geometry is provided by a Br $\alpha$  spectrum shown in Figure 7. The blue shifted component of the emission is much stronger relative to the case for Br $\gamma$ . The longer wavelength emission penetrates the “cap” more than the shorter wavelength does. We interpret the compact emission in #48 as arising in a rotating torus, but some type of shell geometry is possible as well. Indeed there is a weak continuous bridge of emission connecting the torus to the bulk of the extended emission at a point a few arcseconds to the south of the continuum source. The outer extent of this shell feature can be seen in Figure 5 as the lowest contour plotted. There is a corresponding “hole” or lack of emission which is not evident due to the stretch of the image.

The nebular and torus components are not as well separated in the Br $\alpha$  case. Since the

CO mean velocity is clearly redshifted to roughly the same velocity as the bulk of the Br $\gamma$  emission and not the mean velocity of the compact component, it appears the CO emission is not arising in the inner region of the accretion torus, but in a region further out.

#### 4.2. Stellar Wind and Disk Wind Components of the Br $\gamma$ Emission

The emission in the M17 sources is much less intense than for NGC3576 #48, and this is consistent with the fact that the photospheres of both sources have been observed at shorter wavelengths as well (Hanson et al. 1997). The M17 sources are somewhat more evolved than BN, MWC–349, and NGC3576 #48. The central sources have had more time to clear away the over-lying birth material. In the case of M17–268, the observed Br $\gamma$  emission consists of two readily separable components. An extended narrow component which appears roughly uniform in extent (at least on scales of  $\sim \pm 5''$ ) and a spatially compact (i.e. centered on the continuum source) and very broad component. The shape of the compact/broad Br $\gamma$  emission in M17–268 appears as a double-peaked profile. The FWHM of the line is approximately  $480 \text{ km s}^{-1}$  and the separation of the two peaks is  $\sim 176 \text{ km s}^{-1}$ . The background subtracted emission of M17–275 is also broad, but not double-peaked. This source exhibits broad wings with a central component which is  $\sim 130 \text{ km s}^{-1}$  FWHM. The extent of the wings is difficult to judge because of the rather small wavelength coverage provided by a single Phoenix grating setting. Ideally, a larger continuum region should be observed on either side of the line. Comparison of different telluric standards suggests the large scale fluctuations in the continuum should be less than about 3%, so the very broad wings evident in Figure 9 may indeed be real.

The basic features seen in the compact Br $\gamma$  spectra of M17–268 and M17–275 are consistent with the CO emission profiles. The broad, double-peaked emission in M17–268 (Figure 8) corresponds with the broad CO profile, suggesting a more edge-on inclination. Similarly, the narrower prominent emission in M17–275 corresponds to the lower  $v_{\text{sin}i}$  determined from its CO profile. The broad wings of M17–275 could be produced in a fast wind originating at the star. The full extent is difficult to determine, but seems at least to be  $\pm 300 \text{ km s}^{-1}$  and may actually be greater than the full coverage of the spectrum,  $\pm 750 \text{ km s}^{-1}$ . The spectra of M17–268 and NGC3576 #48 may also show weak, but broad wings in emission. Hamann & Simon (1986) could not easily fit the Br emission in MWC 349 to such a wind model, but they were attempting to fit the strong, double-peaked profile (like the prominent shape in Figure 6). Our long slit data with a narrow slit allows for a better attempt at separating components of emission which are likely coming from different spatial scales/mechanisms.

If the broad wings in the M17 sources are due to a stellar wind, then it is expected that the velocity extent seen in #275 should be greater than that seen in #268 since the CO and prominent Br emission suggest the latter has a more edge-on geometry. Figure 10 suggests this may be the case. This figure shows a ratio of the #275 to #268 Br $\gamma$  spectra. The ratio tends to increase at the ends of the spectrum as would be expected if the emission in the wings of both sources is due to a wind.

Hollenbach et al. (1993) and Yorke & Welz (1993) developed models for the photoevaporation of accretion disks around massive stars in order to explain the inferred long life times of ultra compact H II (UCH II) regions based upon their numbers relative to the total numbers of OB stars expected in the Galaxy (Wood & Churchwell 1989). The accretion disk could continually resupply fresh material as the outer layers of the disk are ablated off due to the action of the ionizing continuum of the central star and the ensuing heating of the disk gas; see the recent review by Hollenbach et al. (2000). Kessel, Yorke, & Richling (1998) modeled an 8.4  $M_{\odot}$  star and found that the predicted dust temperatures from such a model do not match the temperatures derived from the observed “unresolved” type of UCH II. Perhaps the observed properties of UCH II regions derive from more than one component (e.g a disk/torus plus envelope). Many of the properties of NGC3576 #48 and MWC 349 are similar to UCH II regions (Barbosa et al. 2003, suggested that NGC3576 #48 is an UCH II region) and both exhibit emission line spectra consistent with an ionized disk/torus. The M17 sources 268 and 275 also show spatially compact Br emission which is consistent with a disk origin (especially 268).

In the model spectra produced by Kessel, Yorke, & Richling (1998), the high velocity wind included in their model is not evident. The lower density in the wind and excitation conditions for the lines they chose to model conspire to “hide” the wind compared to the more prominent emission seen from the disk. Our observed Br spectra of NGC3576 #48 show a clear redshifted wing of higher velocity emission (and perhaps a blue shifted wing as well), and the M17 sources both appear to exhibit very high velocity wings. In all cases, the lower velocity emission is prominent while the “wind” component is seen at lower intensity due to the fact that it is highly dispersed. The spectrum of MWC 349 (Hamann & Simon 1986) was obtained through a much wider aperture than the slit used here (3.75”) and this could further dilute the presence of a wind. The nature of these wings should be investigated further with longer wavelength coverage and detailed wind plus disk models.

### 4.3. Timescales and the Accretion Process

The ionizing radiation from massive stars, coupled with a stellar wind is expected to have a profound effect on a circumstellar disk (Hollenbach et al. 2000). Richling & Yorke (1997) calculated the disk dispersal times for B-type stars (appropriate to the types of central stars discussed here) from detailed hydrodynamical models. For a wide range of mass loss properties, the dispersal time for early B-type stars with ionizing continuum luminosities up to  $\sim 10^{48} \text{ s}^{-1}$ , is between  $10^5$  and a few  $10^6$  yr.

We have carried out a survey of massive star clusters embedded in giant H II (GHII) regions in the Galaxy (Blum et al. 1999, 2000, 2001; Figuerêdo et al. 2002, 2004). Coupled with the work of Hanson et al. (1997) in M17, several observations can be made about the timescales for disk dispersal as a function of mass on the zero age main sequence (ZAMS) and/or the formation mechanism for massive stars. This survey covers the most luminous GHII in the Galaxy as tabulated by Smith et al. (1978). Because massive star clusters will naturally disperse their birth material as they evolve, these luminous clusters must be young.

While the survey is not yet complete (specifically, we have yet to obtain near infrared spectra for the brightest members of all the GHII stellar clusters), to-date we find that in each case where mid to early O-type stars (i.e. the most massive stars) are revealed in the cluster, only second rank late O or early B stars exhibit signatures of circumstellar envelopes or disks/tori (W31, W43, W42, and M17 from Hanson et al. 1997). In no cluster in the survey (nor any other reported in the literature to our knowledge) has a young *massive* O star been found which has the clear disk signatures seen in the lower mass OB stars such as those presented here (i.e. the classic CO emission profile). This may naturally be due to a shorter dispersal time scale for the more energetic stars; on the other hand, it is also consistent with a difference in formation mechanism for the most massive stars—they may form by collisional processes instead of pure accretion.

In the former case, the models of Richling & Yorke (1997) suggest the stars in our sample are less than about 1 Myr old. The models and the observed lack of massive O stars with similar disk signatures suggest the dispersal timescale must be quite short, perhaps significantly less than  $10^5$  yr. Clearly, higher mass detailed models would be very useful. The near infrared observations may be approaching their limit for massive stars. If the timescale for dispersal is so short, then the prospect of observing the inner accretion disk in CO at these wavelengths for massive O stars is diminished since the overlying envelope may completely obscure the inner regions.

## 5. SUMMARY

We have presented high dispersion near infrared spectra of a sample of massive stars still involved in the birth process and embedded within massive star clusters. The spectra reveal CO 2.3  $\mu\text{m}$  2–0 rotational–vibrational bandhead profiles which are well fit by a rotating Keplarian disk for three of the four stars in the sample. For the fourth, NGC3576 #48 which exhibits a narrow CO profile, other circumstellar geometries are possible. In particular, we present evidence that the CO emission in this case may arise in a region between the expanding cavity surrounding the central source and its more compact accretion torus. Similar mechanisms may be at work in the more well known BN and MWC 349 objects.

The CO profiles in three of our four stars provide solid evidence that massive stars do indeed form by accretion. Together with similar CO profiles presented by Chandler et al. (1995) for two early B–type stars, it is clear that stars as massive as 10–30  $M_{\odot}$  form with accretion disks just as for lower mass stars. The timescale for disk dispersal by the ionizing and wind action of massive stars must be quite short for the most massive stars in Galactic young clusters because none has been observed with a similar signature as that for the second rank OB stars. Alternately, the formation mechanism for the most massive stars may be different.

CLB and AD thank FAPESP and PRONEX for support. PSC appreciates continuing support from the National Science Foundation. We appreciate the critique of an anonymous referee which has helped to improve our paper.

## REFERENCES

- Barbosa, C. L., Daminieli, A., Blum, R. D., & Conti, P. S. 2003, *AJ*, 126, 2411
- Behrend, R. & Maeder, A. 2001, *A&A*, 373, 190
- Bevington, P. R. & Robinson, D. K. 1992, “Data Reduction and Error Analysis for the Physical Sciences,” MacGraw–Hill, New York, p147.
- Blum, R.D., Daminieli, A., & Conti, P.S. 1999, *AJ*, 117, 1392
- Blum, R.D., Conti, P.S., & Daminieli, A. 2000, *AJ*, 119, 1860
- Blum, R. D., Daminieli, A., Conti, P. S. 2001, *AJ*, 121, 3149
- Bonnell, I. A., Bate, M. R., & Zinnecker, H. 1998, *MNRAS*, 298, 93
- Bonnell, I. A. & Bate, M. R. 2002, *MNRAS*, 336, 659
- Carr, J. S. 1989, *ApJ*, 345, 522
- Carr, J. S., Tokunaga, A. T., Najita, J., Shu, F. H., & Glassgold, A. E. 1993, *ApJ*, 411, L37
- Chandler, C. J., Carlstrom, J. E., Scoville, N. Z., Dent, W. R. F., & Geballe, T. R. 1993, *ApJ*, 412, L71
- Chandler, C. J., Carlstrom, J. E., & Scoville, N. Z. 1995, *ApJ*, 466, 793
- Conti, P. S. & Blum, R. D. 2002, *ApJ*, 564, 827
- Churchwell, E. 2002, *ARA&A*, 40, 27
- De Buizer, J. M. 2003, *MNRAS*, 341, 277
- Dent, W. R. F. & Geballe, T. R. 1991, *A&A*, 252, 775
- de Pree, C. G., Nysewander, M. C., & Goss, W. M. 1999, *AJ*, 117, 2902
- Figer, D. F., McLean, I. S., & Najarro, F. 1997, *ApJ*, 486, 420
- Figuerêdo, E., Blum, R. D., Daminieli, A., Conti, P. S. 2002, *AJ*, 124, 2739
- Figuerêdo, E., Blum, R. D., Daminieli, A., Conti, P. S. 2004, in preparation
- Garay, G. & Lizano, S. 1999, *PASP*, 111, 1049
- Hamann, F. & Simon, M. 1986, *ApJ*, 311, 909

- Hanson, M. M., Conti, P. S., & Rieke, M. J. 1996, *ApJS*, 107 281
- Hanson, M. M., Howarth, I.D., & Conti, P.S. 1997, *ApJ*, 489, 698
- Hanson, M. M., Rieke, G., & Luhman K. L. 1998, *AJ*, 116 1915
- Hillenbrand, L. A., Strom, S. E., Vrba, F. J., & Keene, J. 1992, *ApJ*, 397, 613
- Hinkle, K., Wallace, L., & Livingston, W. 1995, *PASP*, 107, 1042
- Hinkle, K. H. et al. 2003, *Proc. SPIE*, 4834, 353
- Hollenbach, D., Johnstone, D., & Shu, F. 1993, *ASP Conf. Ser.* 35: *Massive Stars: Their Lives in the Interstellar Medium*, 26
- Hollenbach, D., Johnstone, D., Lizano, S., & Shu, F. 1994, *ApJ*, 428, 654
- Hollenbach, D. J., Yorke, H. W., & Johnstone, D. 2000, *Protostars and Planets IV*, 401
- Kessel, O., Yorke, H. W., & Richling, S. 1998, *A&A*, 337, 832
- Kraus, M., Krügel, E., Thum, C., & Geballe, T. R. 2000, *A&A*, 362, 158
- Kurtz, S., Cesaroni, R., Churchwell, E., Hofner, P., Walmsley, M. 2000, in *Protostars and Planets IV.*, eds Mannings, V., Boss, A. P., Russell, S. S. (Tucson:University of Arizona Press), p. 299
- Mathis, J.S. 1990, *ARA&A*, 28, 37
- McKee, C. F. & Tan, J. C. 2003, *ApJ*, 585, 850
- Najita, J., Carr, J. S., Glassgold, A. E., Shu, F. H., & Tokunaga, A. T. 1996, *ApJ*, 462, 919
- Norris, R. P. et al. 1998, *ApJ*, 508, 275
- Phillips, C. J., Norris, R. P., Ellingsen, S. P., & McCulloch, P. M. 1998, *MNRAS*, 300, 1131
- Richling, S. & Yorke, H. W. 1997, *A&A*, 327, 317
- Rodríguez, L. F. & Bastian, T. S. 1994, *ApJ*, 428, 324
- Scoville, N., Kleinmann, S. G., Hall, D. N. B., & Ridgway, S. T. 1983, *ApJ*, 275, 201
- Shepherd, D. S. & Kurtz, S. E. 1999, *ApJ*, 523, 690
- Smith, L.F., Biermann, P. & Mezger, P.G. 1978, *A&A*, 66, 65



- Stahler, S. W., Palla, F., & Ho, P. T. P. 2000, *Protostars and Planets IV*, 327
- Vacca, W. D., Garmany, C. D., & Shull, J. M. 1996, *ApJ*, 460, 914
- Walsh, A. J., Burton, M. G., Hyland, A. R., & Robinson, G. 1998, *MNRAS*, 301, 640
- Wood, D. O. S. & Churchwell, E. 1989, *ApJS*, 69, 831
- Yorke, H. W. & Welz, A. 1993, in *Star Formation, Galaxies, and the Interstellar Medium*, eds J. Franco, F. Ferrini, and G. Tanorio-Tagle (Cambridge University Press), p318
- Yorke, H. W. & Sonnhalter, C. 2002, *ApJ*, 569, 846

Table 1. Table of Observations

Object	Date <sup>a</sup>	Line	$K$	$H - K$	Reference <sup>b</sup>
NGC3576 #48	Feb 14, 2002; Feb 17, 2003	CO	8.35	2.21	Figuerêdo et al. (2002)
NGC3576 #48	April 18, 2003	Br $\gamma$ , Br $\alpha$			Figuerêdo et al. (2002)
M17 #268	May 11, 2003	CO, Br $\gamma$	9.6	1.0	Hanson et al. (1997)
M17 #275	May 11, 2003	CO, Br $\gamma$	8.0	1.2	Hanson et al. (1997)
G333.1-0.4 #4	July 29, 2003	CO	10.92	1.44	Figuerêdo et al. (2004)

<sup>a</sup>UT Date of the observations.

<sup>b</sup>Reference presenting object photometry, low resolution spectra, object coordinates, and finding chart.

Table 2. CO Line Profile Parameters and Stellar Properties

Object	$p^a$	$q^b$	$\beta^c$	Model CO Line Width <sup>d</sup> (km s <sup>-1</sup> )	$N_{\text{CO}}^e$ (10 <sup>21</sup> cm <sup>-2</sup> )	$v\text{sini}^f$ (km s <sup>-1</sup> )	$V_o^g$ (km s <sup>-1</sup> )	Mass <sup>h</sup> ( $M_\odot$ )	Luminosity ( $L_\odot$ )
NGC3576 #48	0.5	$1.0 \pm 0.03$	$2.1 \pm 0.04$	1.0	$13.4 \pm 0.1$	$25.0 \pm 0.2$	$-21.5 \pm 1.3$ <sup>i</sup>	17 <sup>j</sup>	>50000 <sup>j</sup>
M17 #268	0.5	$3.8 \pm 0.1$	$5.8 \pm 0.1$	1.0	$22.3 \pm 1.8$	$258.7 \pm 1.9$	$0.0 \pm 1.3$	10	5000
M17 #275	0.5	$4.1 \pm 0.1$	$6.9 \pm 0.3$	1.0	$3.5 \pm 0.2$	$109.7 \pm 0.6$	$-7.0 \pm 1.3$	15	20000
G333.1-0.4 #4	0.5	$3.6 \pm 0.3$	$6.5 \pm 1.0$	1.0	$1.3 \pm 0.4$	$108.0 \pm 1.9$	$-26.0 \pm 1.4$	5 <sup>j</sup>	>300 <sup>j</sup>

<sup>a</sup>Temperature power-law exponent where  $T = T_o (r/r_i)^{-p}$ .  $T_o = 5000$  K for all models and  $r_i$  is the inner radius of CO emission zone.

<sup>b</sup>Surface Density,  $\Sigma$ , power-law exponent where  $\Sigma = N_{\text{CO}} (r/r_i)^{-q}$  and  $r_i$  is the inner radius of CO emission zone.

<sup>c</sup>Ratio of the outer to inner radius of the CO emission zone.

<sup>d</sup>The intrinsic line width at a point in the disk. The models adopt Lorentzian profiles as in Najita et al. (1996), but Gaussian profiles of larger width can also fit the data.

<sup>e</sup>Surface density at the inner edge of the CO emission zone.

<sup>f</sup>The projected rotational velocity of the Keplerian disk at the inner edge of the CO emission zone.

<sup>g</sup>Velocity shift from rest wavelength. Not corrected to heliocentric velocity.

<sup>h</sup>Stellar mass derived from luminosity and associated spectral type (see reference listed in Table 1). For the M17 sources, the mass comes from the placement in the H-R diagram. For the remaining sources, the mass is estimated from the ZAMS tabulation of Hanson et al. (1997).

<sup>i</sup>The radio recombination line velocity of NGC3576 is given as  $-24$  km s<sup>-1</sup> by de Pree et al. (1999) and is consistent with the velocity of the bulk of the extended Br $\gamma$  emission #48. The mean observed CO velocity corresponds to a Heliocentric velocity of  $-8.8$  km s<sup>-1</sup>. See also Table note *a* of Table 3.

<sup>j</sup>Approximate lower limit to the source luminosity and mass derived by assuming an approximate maximum excess emission; see reference quoted in Table 1.

Table 3. Observed Br $\gamma$  Emission Velocities

Object	$V_o^a$ (km s $^{-1}$ )	FWHM $^b$ (km s $^{-1}$ )	P2P $^c$ (km s $^{-1}$ )
NGC3576 #48	$-66 \pm 1$	$124 \pm 5$	$84 \pm 1$
M17 #268	$5 \pm 2$	$477 \pm 7$	$166 \pm 6$
M17 #275	$-16 \pm 2$	$121 \pm 3$	

<sup>a</sup>Mean velocity of compact emission, e.g., the “torus” or “disk wind” component. Compare to values given in Table 2 for the mean CO emission velocity. This is the observed velocity. For #48 the Heliocentric velocity is within 1 km s $^{-1}$  of the observed velocity. For the M17 sources the Br $\gamma$  and CO data were obtained on the same night, so they are directly comparable. The quoted errors are dominated by the continuum choice; see text.

<sup>b</sup>Full width at half maximum for the same component as  $a$ . The quoted errors are dominated by the continuum choice; see text

<sup>c</sup>Peak-to-peak velocity separation for the torus or disk wind components in NGC3576 #48 (Figure 6 and M17-268 (Figure 8).

.

.

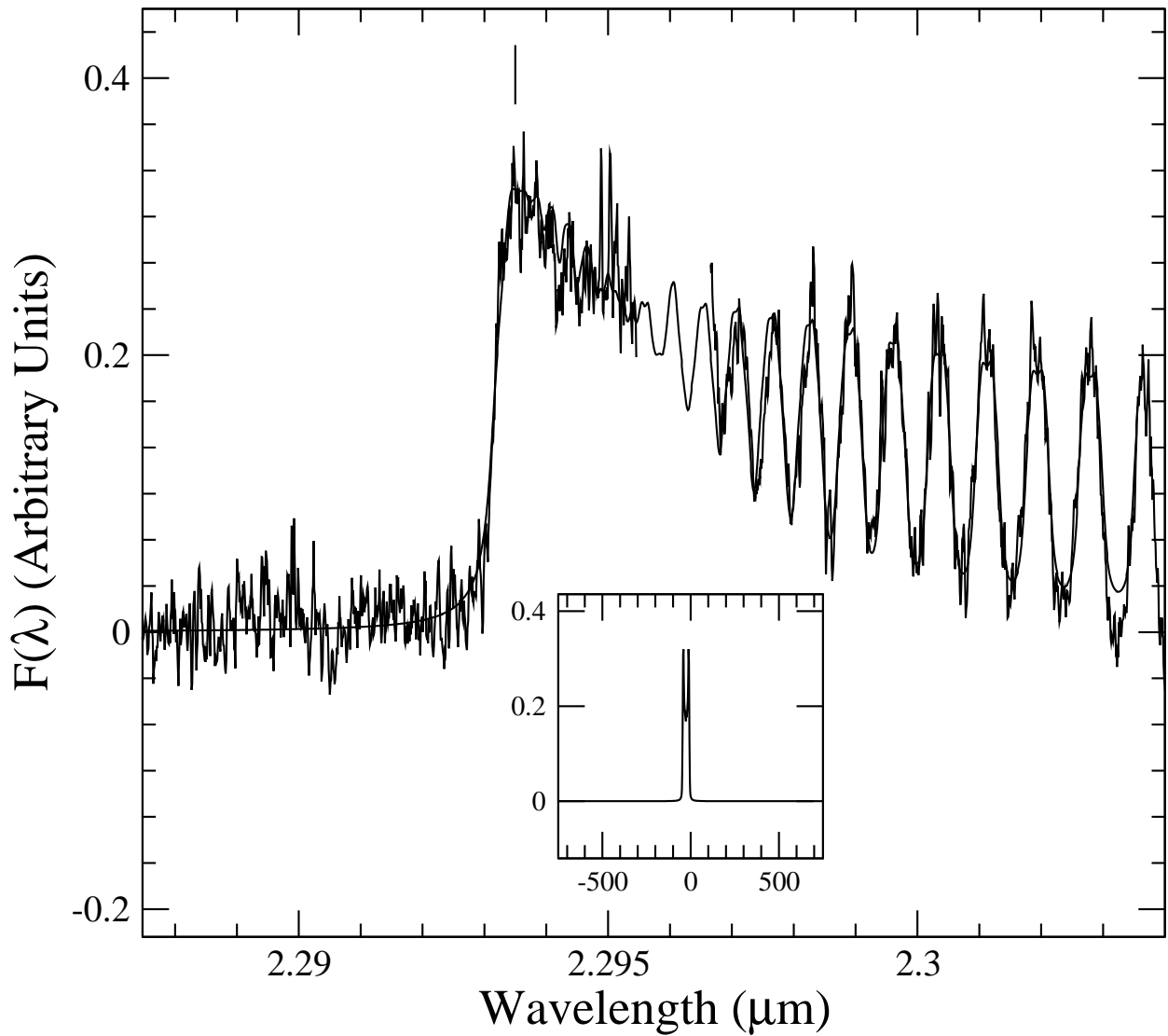


Fig. 1.— The CO 2-0 first overtone rotational–vibrational bandhead for source #48 in NGC3576. The smooth curve is a model for the emission profile arising from a Keplerian disk (see text and Table 2). The spectrum is a sum of two grating settings. The region near 2.296  $\mu\text{m}$  is the interface between the two, and the array has a number of bad pixel rows on one end of the detector making the spectrum here unreliable, and it has been masked out in this figure. The short vertical line marks the vacuum rest wavelength of the bandhead (2.2935  $\mu\text{m}$ ), and the inset shows the emission–line profile for a single line in the bandhead ( $v = 2-0$ ,  $J = 51-50$ ). The  $x$  axis of the inset is in  $\text{km s}^{-1}$  and is one Phoenix grating setting in extent.

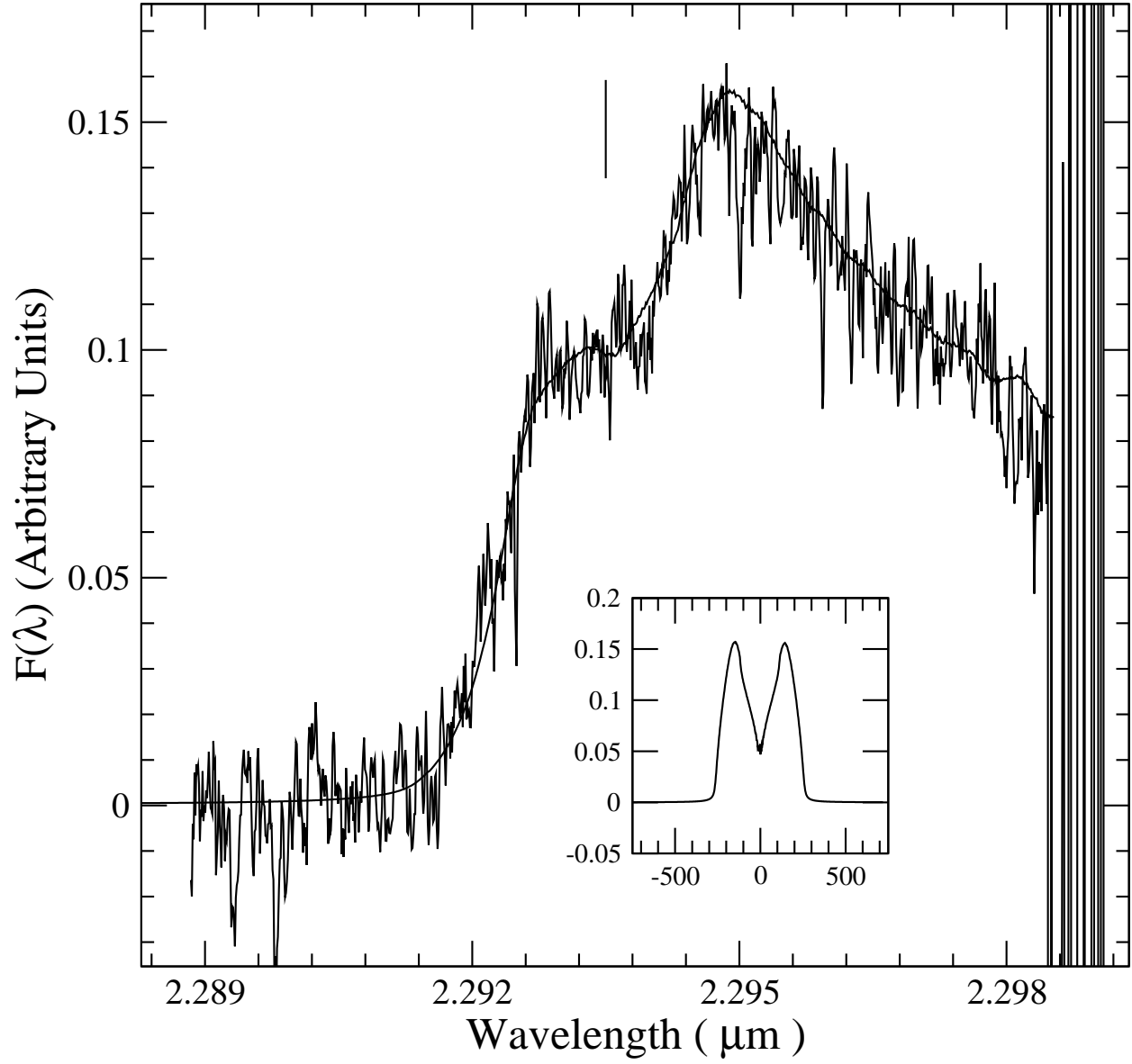


Fig. 2.— Same as Figure 1 but for source 268 in M17.

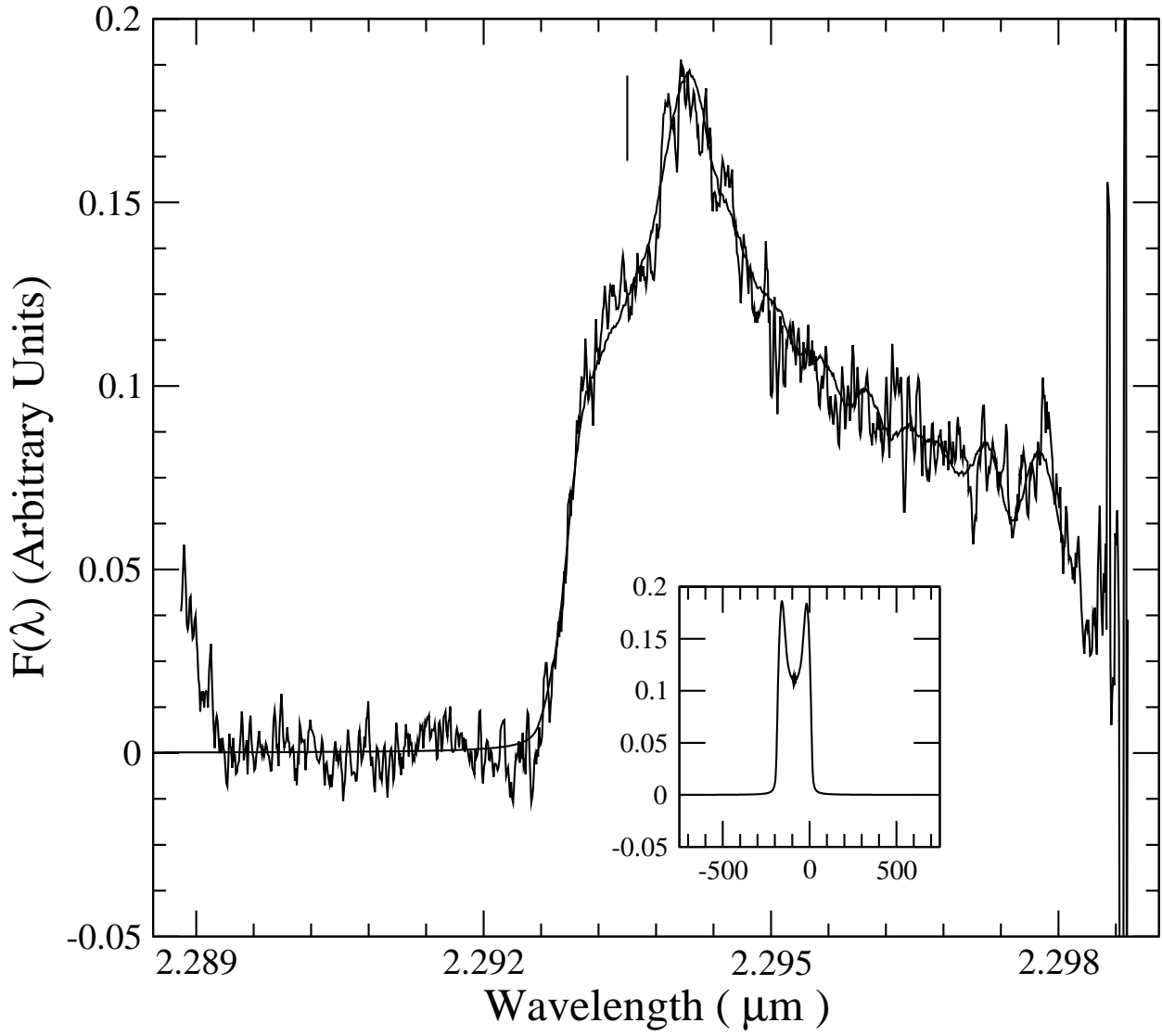


Fig. 3.— Same as Figure 1 but for source 275 in M17.



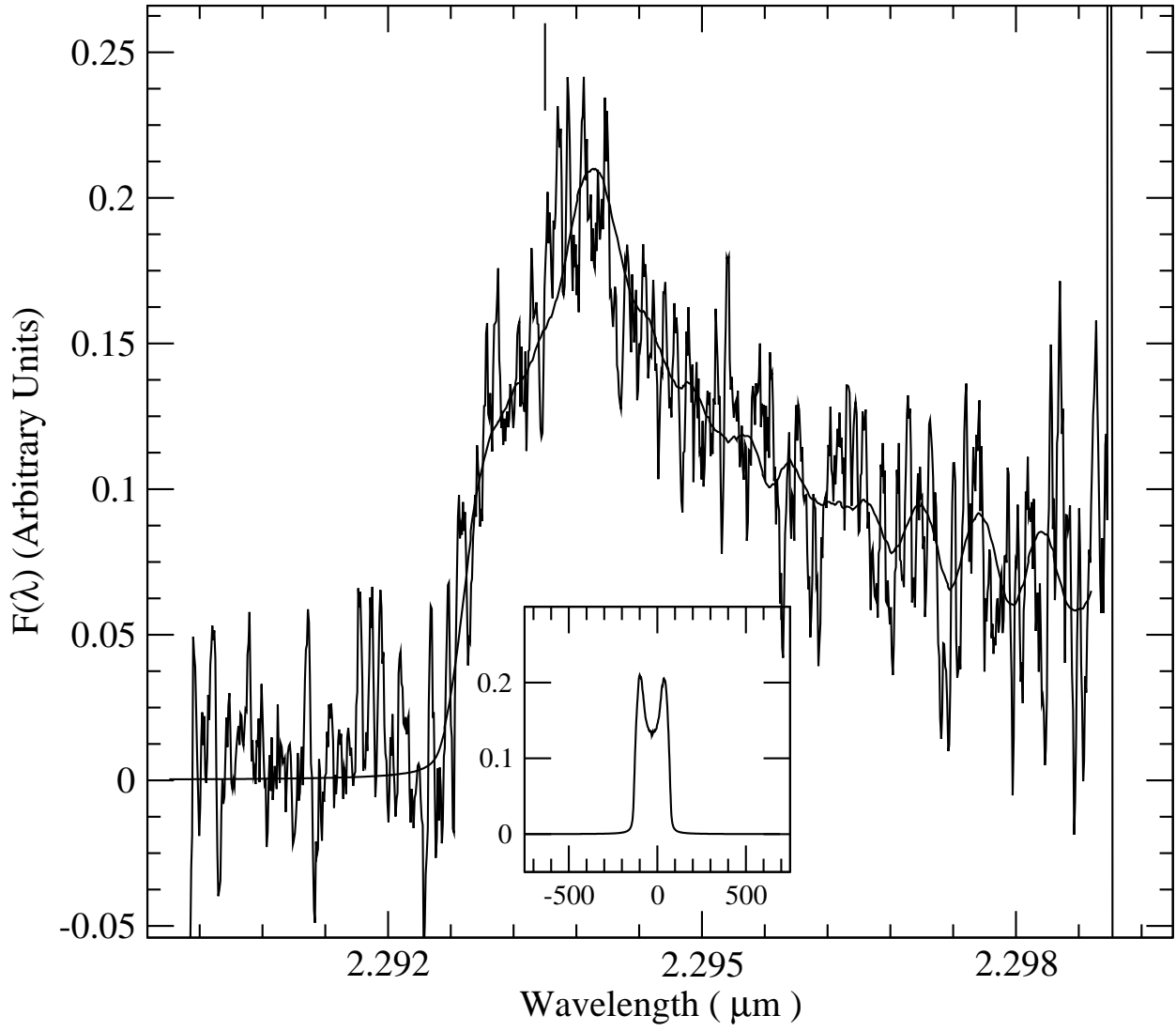


Fig. 4.— Same as Figure 1 but for source #4 in G333.1-0.4.

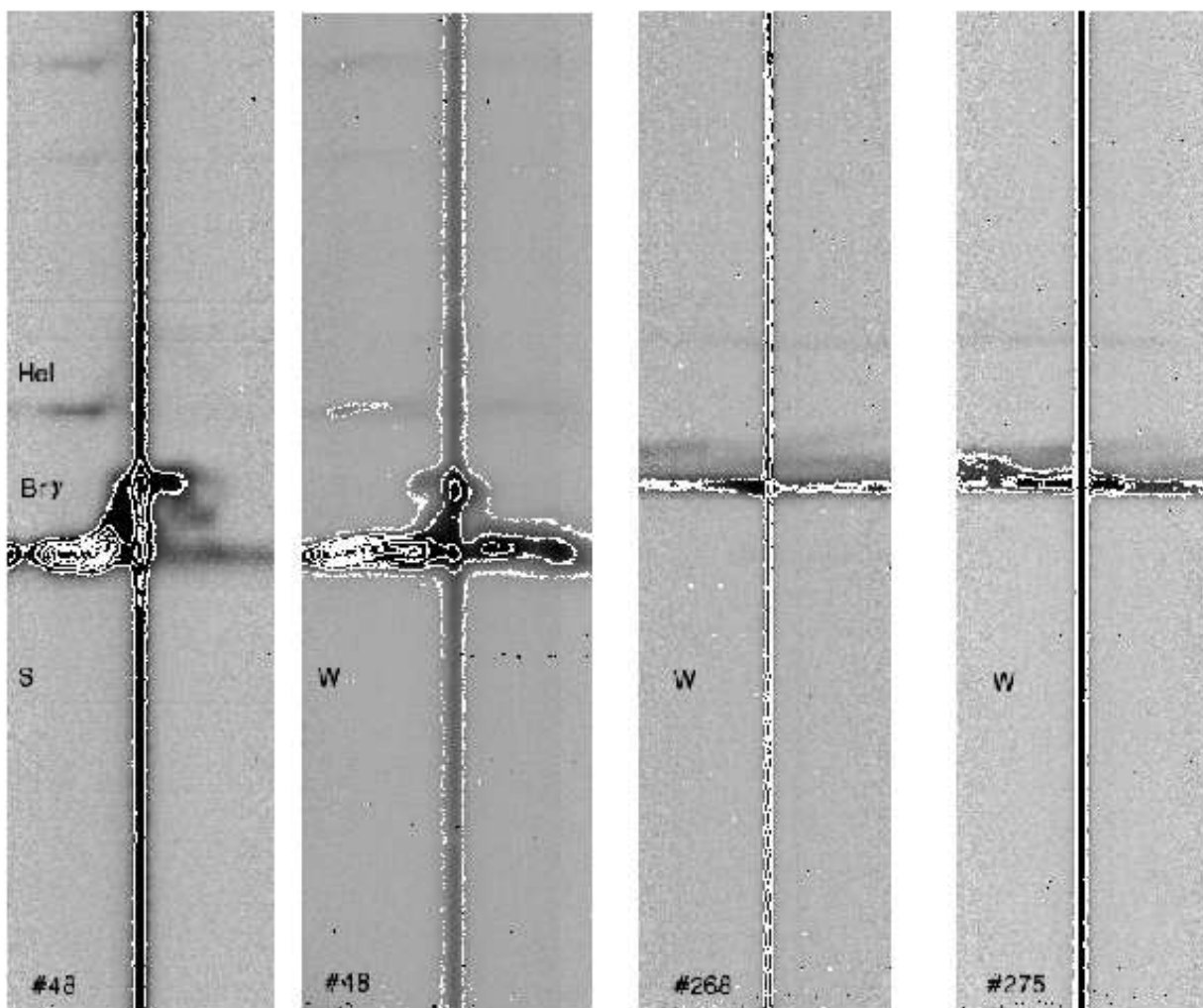


Fig. 5.— Two dimensional long slit images in the  $\text{Br}\gamma$  grating position for the NGC3576 #48, and the M17 sources: *far left*, N-S slit for NGC3576 #48, *middle left*, E-W slit for NGC3576 #48, *middle right*, M17-268, *far right*, M17-275. West and South are to the *left* in these images. The spatial dimension is along the horizontal axis in each image and covers approximately  $20''$ – $24''$  along the slit. The images are combinations of the individual dither positions. The vertical axis is the dispersion (or spectral) dimension, and its velocity extent is approximately  $1500 \text{ km s}^{-1}$  for each image. He I 7-4 emission is present in each case to the blue of  $\text{Br}\gamma$  (both lines marked in the #48 N-S image). The HeI emission has a compact component (i.e. superimposed on the continuum source) just as does the  $\text{Br}\gamma$  emission; see Figure 6 and text. The contours (derived from the same images) are overlaid on the gray scale to give an indication of the relative strength of the emission along the slit and compared to the continuum source.

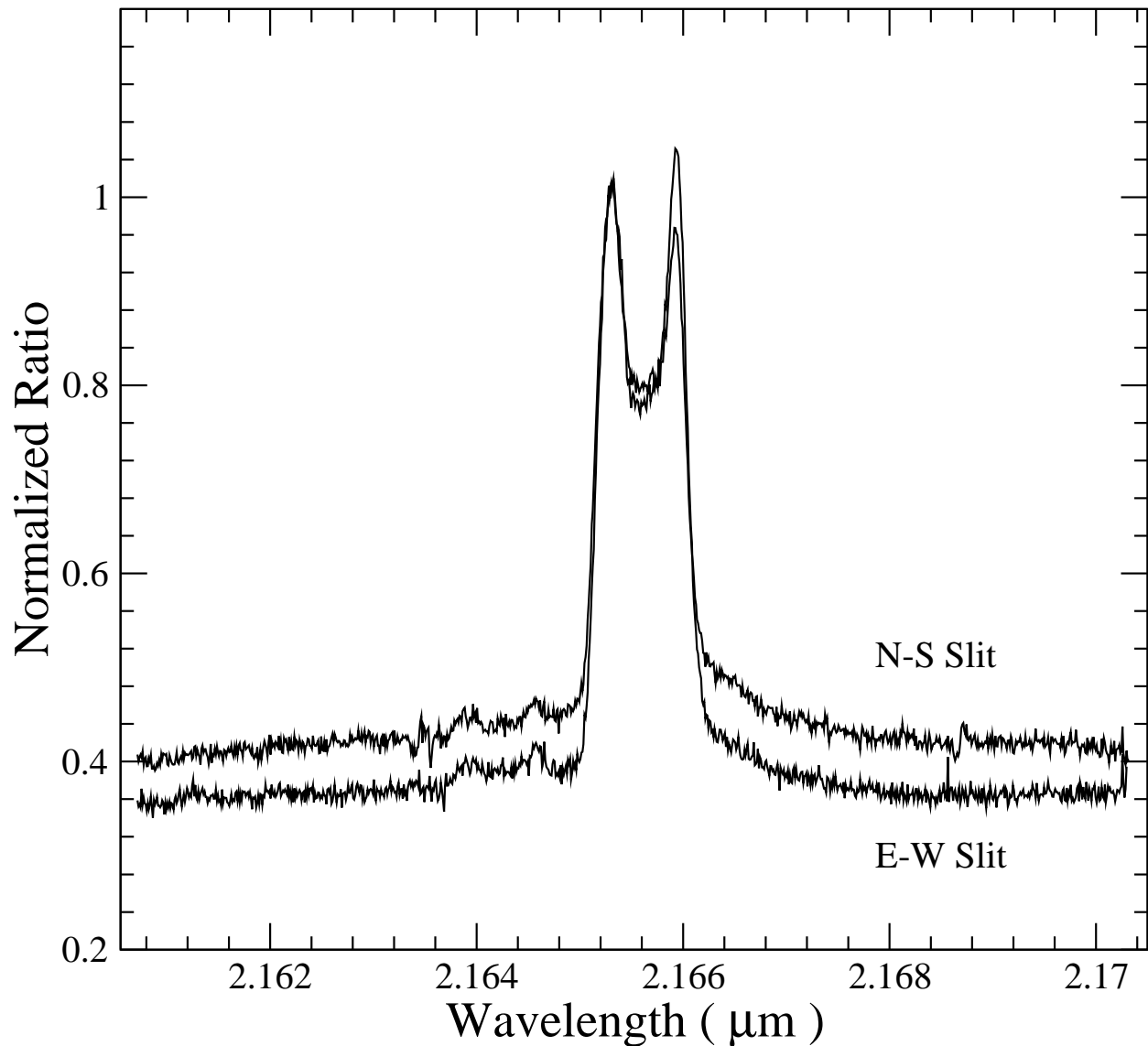


Fig. 6.— Br $\gamma$  emission for source #48 in NGC3576. The two curves represent the emission seen through the Phoenix 0.32'' slit and summed over pixels corresponding to 0.9'' along the slit spatial dimension. No nebular background is subtracted from these spectra because it is strong and variable away from the source. The two spectra were obtained with different slit orientations. The lower spectrum had an E-W slit while the upper had N-S.

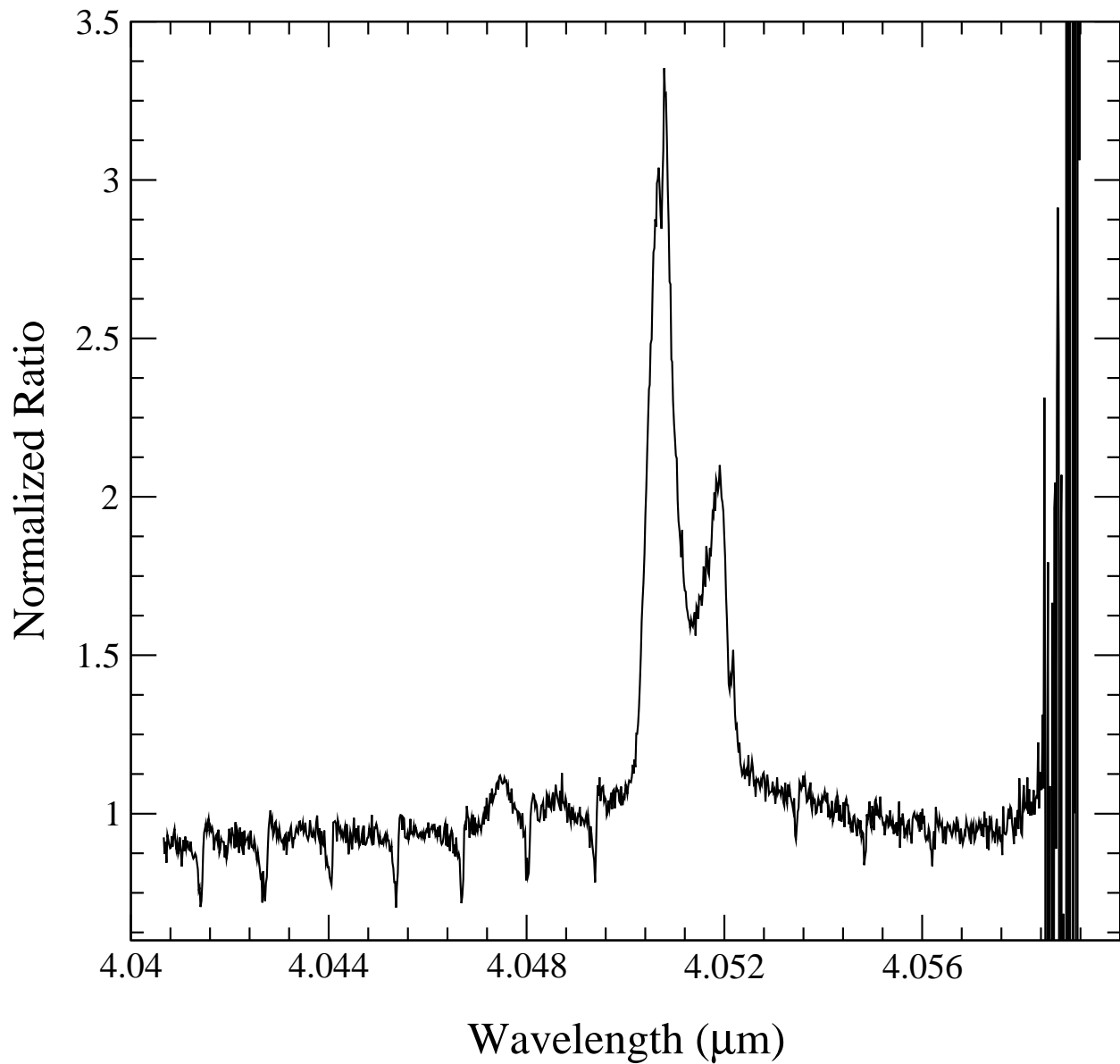


Fig. 7.— Same as Figure 6 but for  $\text{Br}\alpha$  ( $4.052 \mu\text{m}$ ). No background has been subtracted. The slit orientation is N–S. The blue shifted component is stronger than in the  $\text{Br}\gamma$  case because the longer wavelength emission is less affected by the intervening dust; in this case, the emission arises from the inner wall of the cavity surrounding NGC3576 #48 (see text). The blue peak, in particular is contaminated by the spatially extended component of emission. The “absorption” features are due to incomplete telluric correction.

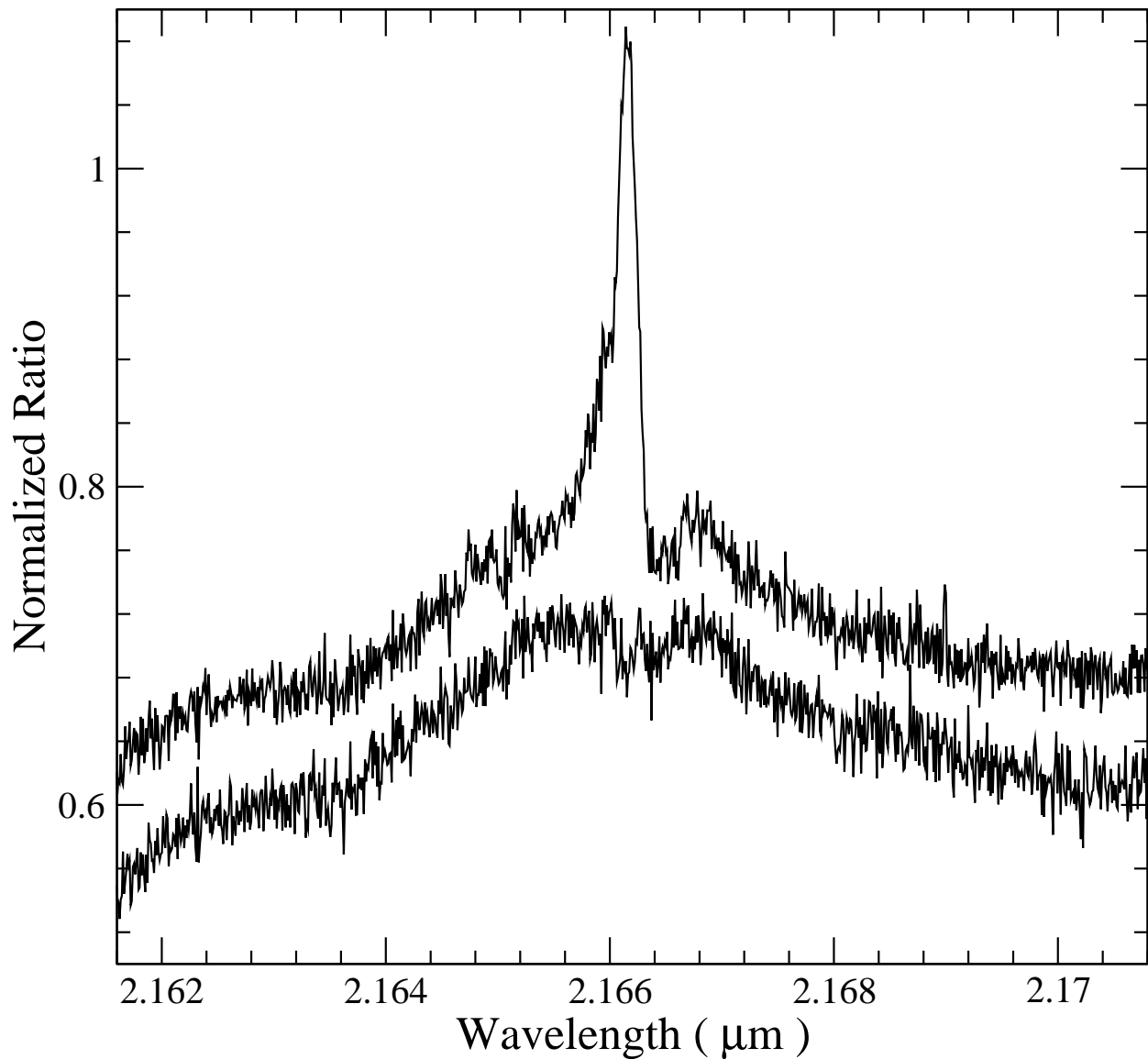


Fig. 8.—  $\text{Br}\gamma$  emission for M17-268. The upper curve represents the total emission seen through the Phoenix  $0.32''$  slit and summed over pixels corresponding to  $0.4''$  along the slit spatial dimension. The lower curve is the same except that the background has been subtracted from nearby ( $\sim \pm 1''$ ) apertures. The two curves are nearly identical except for the narrow blue emission peak and have been separated vertically for clarity. The clean subtraction of the blue peak highlights the uniformity of the background across the source. The background subtracted spectrum has a broad, double-peaked profile consistent with disk emission. The profile is approximately  $450 \text{ km s}^{-1}$  wide at half the peak intensity.

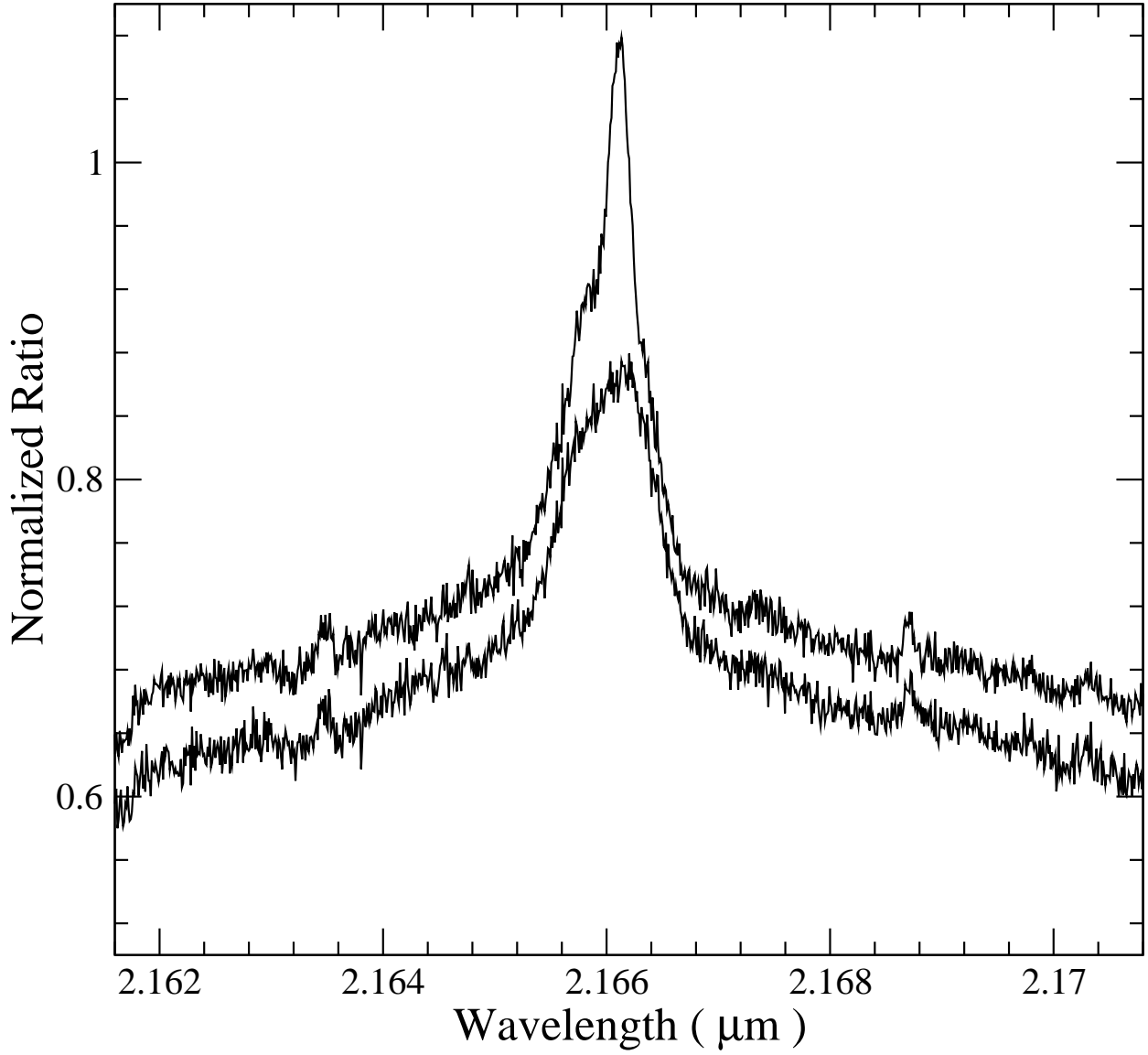


Fig. 9.— Same as Figure 8 but for M17-275.

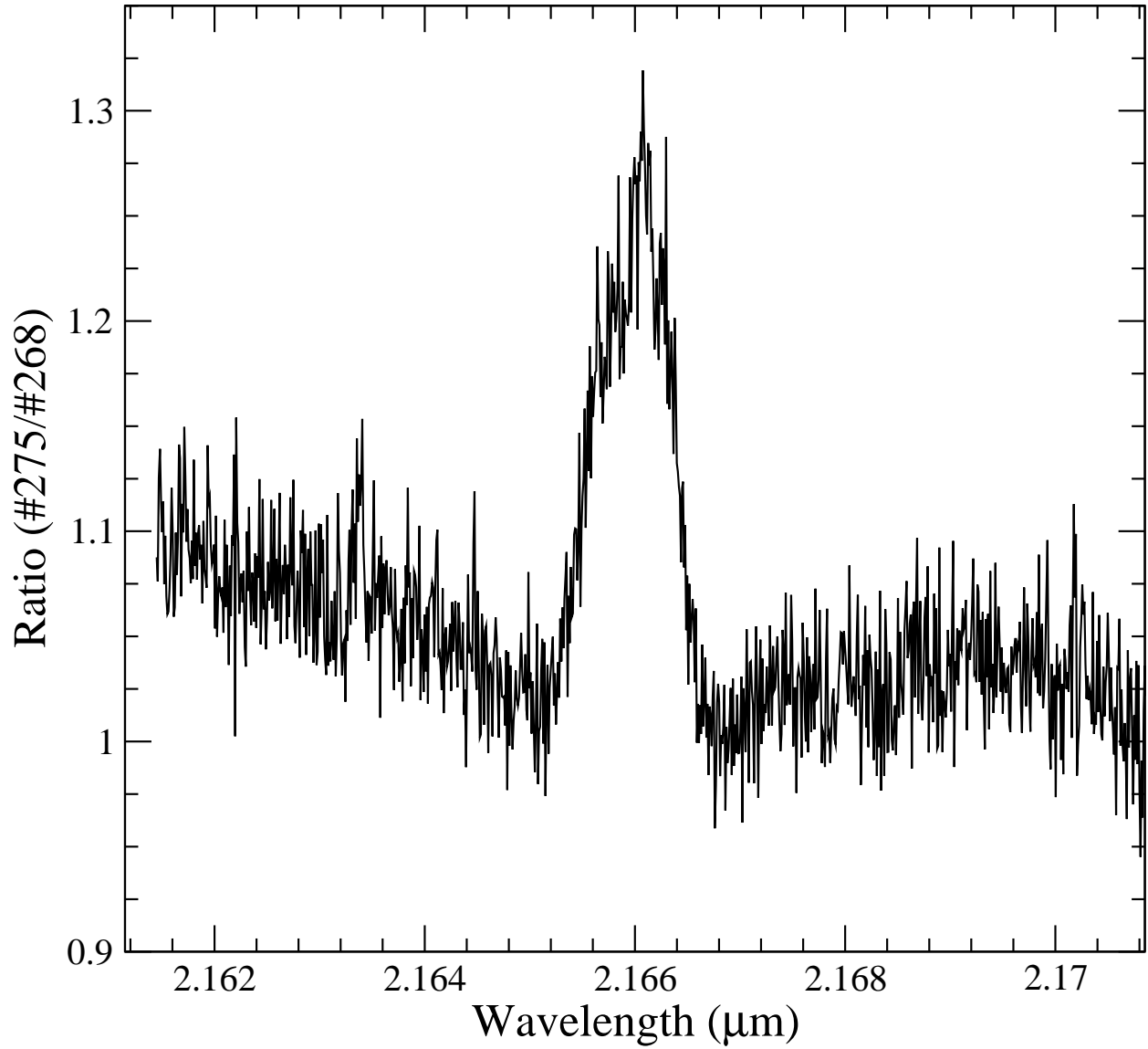


Fig. 10.— Ratio of background subtracted M17 sources (275/268). The increasing ratio in the wings of the spectra is consistent with a larger velocity extent in #275. This would be expected if the wings are due to a fast wind since #275 has a more face-on geometry.